Confinement and manipulation of non-neutral plasmas using rotating wall electric fields

E. M. Hollmann, F. Anderegg, and C. F. Driscoll
Physics Department and Institute for Pure and Applied Physical Sciences, University of California at San Diego, La Jolla, California 92093-0319

(Received 24 February 2000; accepted 17 April 2000)

A ''rotating wall'' perturbation technique enables confinement of up to 3×10^9 electrons or 10^9 ions in Penning–Malmberg traps for periods of weeks. These rotating wall electric fields transfer torque to the particles by exciting Trivelpiece–Gould plasma modes with $k_z\neq0$ and $m_\theta=1$ or 2. Modes that rotate faster than the plasma column provide a positive torque that counteracts the background drags, resulting in radial plasma compression or steady-state confinement in near-thermal equilibrium states. Conversely, modes that rotate slower than the plasma provide a negative torque, and enhanced plasma expansion is observed. The observed Trivelpiece–Gould mode frequencies are well predicted by linear, infinite-length, guiding-center theory. © *2000 American Institute of Physics.* [S1070-664X(00)05407-0]

I. INTRODUCTION

Penning traps are used for the confinement of single species electron or ion plasmas for a range of experiments in plasma physics,[1] atomic physics,[2] and antimatter research.[3] A uniform magnetic field in the axial direction gives radial confinement, and voltages applied to end electrodes provide axial confinement of a single sign of charge. These traps have long inherent confinement times because of the conservation of total angular momentum P_θ in a cylindrically symmetric trap.

In practice, background neutral gas and asymmetries inherent in the trap construction break the cylindrical symmetry and exert a drag on the rotating plasma; this drag causes radial expansion and eventual particle loss. In Penning–Malmberg traps, the cylindrical confinement electrodes can be varied in length, and the asymmetry-induced losses are observed to increase with plasma length.[4] In general, the radial expansion and loss can be counteracted by applying an external torque: steady-state confinement is achieved when the applied torque counterbalances the inherent drag, and plasma compression occurs when the applied torque is larger than the inherent drag.

Two methods which have been used previously to compress plasmas in Penning traps are laser torquing and ''sideband cooling.'' In laser torquing, a laser beam aimed at the edge of an ion plasma transfers momentum from the beam to the plasma. This method requires an accessible atomic transition, and is thus limited to a small number of ion species. Also, fluctuations in laser power, frequency, and pointing can make this method difficult to implement. Nevertheless, laser torquing has provided steady-state confinement of 10^3–10^6 Be^+ ions in harmonic Penning traps.[5]

In side-band cooling, an applied oscillating electric field parametrically couples the azimuthal ''magnetron'' motion to the axial bounce motion of a small number of particles in harmonic Penning traps. Resistive cooling of the bounce motion then causes cooling of the magnetron motion, with consequent radial compression. This method becomes ineffective for large trapped plasmas, because the magnetron motion and collective bounce motion become dominated by plasma space-charge effects. Side-band cooling has been used to compress 10^3–10^4 electrons in harmonic Penning traps.[6]

It is well known that plasma waves can greatly enhance particle transport. Both spheroidal plasmas and long plasmas show strong confinement degradation when applied stationary perturbations coincide with a plasma mode.[5,7] In long electron plasmas, modest density and angular momentum increases were reported[8] when the applied perturbation excited a plasma mode, but strong heating was observed and background ionization made the technique impractical at low magnetic fields ($B\leqslant400$ G).

The first practical development of compression and steady-state confinement by ''rotating wall'' fields was for Mg^+ ions in a long Penning–Malmberg trap.[9] Here, the rotating voltage perturbation was applied to a sectored electrode comprising about 20% of the confinement length. Up to 10^9 ions were held near global thermal equilibrium, i.e., with near-uniform temperature, density, and rotation frequency, for periods of weeks. The plasma rotation frequency was observed to be somewhat less than the rotation frequency of the wall perturbation, and the ''slip'' between the two was observed to depend on temperature. However, no clear signature of mode resonances was seen in the original experiments.

In other experiments at the National Institute of Standards and Technology, Boulder,[10] a modification of this rotating wall technique provided steady-state confinement for small (about 10^6 ions) spheroidal Be^+ plasmas in harmonic Penning traps. In this case, the rotating wall perturbation had essentially no axial dependence in the plasma ($k_z\approx0$). The Be^+ ions were laser-cooled to a strongly-correlated state ($T\simeq10$ mK), and were observed to rotate with zero slip, i.e. phase locked to the applied rotating field. Separately, com-

pression of these small spheroidal plasmas was obtained by driving $k_z=0$ cyclotron modes.[11] This mode-enhanced drive gave larger torques, but also larger heating, than the phase-locked drive. Also, confinement degradation and heating have been observed when $k_z\neq 0$ modes have zero frequency in the lab frame, and thus are resonant with static field errors.[5,7]

The first implementation of the rotating wall technique on an electron plasma[12] identified the $k_z\neq 0$ Trivelpiece–Gould (TG) plasma modes as the dominant mechanism coupling the rotating wall to the plasma. Here, we show that a $k_z\neq 0$ rotating wall perturbation couples to both electron plasmas and ion plasmas predominantly through excitation of these TG plasma modes. The rotating electric field of the wall voltage excites nonazimuthally symmetric TG modes. These TG modes carry angular momentum, which is presumably transferred to the particles by a wave–particle coupling such as Landau damping.

Here, the plasmas consist of up to 3×10^9 electrons or 10^9 Mg^+ ions, and the rotating wall drive provides density compression and steady-state confinement at central densities up to 10^9 cm^{-3} (electrons) and 5×10^8 cm^{-3} (ions). We find that a torque large enough to counteract the inherent drag is observed only when the rotating wall frequency is chosen such that an electrostatic Trivelpiece–Gould mode with axial dependence ($k_z\neq 0$) and azimuthal dependence ($m_\theta\neq 0$) is excited in the plasma. TG modes rotating faster than the plasma are found to cause a positive torque, while modes rotating slower than the plasma are found to cause a negative torque (drag) on the plasma. We note that these experiments emphasize the importance of wave resonances in determining the fields and torque on the plasma; but they do not elucidate the microscopic field/particle interactions required for wave damping and torque absorption.

These experiments were performed on electron plasmas with temperatures $0.2<T<2$ eV and on ion plasmas with temperatures $10^{-4}<T<4$ eV. The frequencies of the modes studied here are a small fraction of the plasma frequency ω_p (since $k_z\ll 2\pi/R_w$) and are typically slightly higher than the **E×B** drift frequency. The observed frequencies of these modes are found to be well predicted by linear, infinite-length, guiding-center theory.

This paper is organized as follows: First, the general experimental setup is described. Although the same apparatus is used for both electron and ion experiments, the diagnostics and parameters are distinct, and are given separate descriptions. The basic model used here to predict the Trivelpiece–Gould mode frequencies is then outlined. Measurements of mode frequencies obtained from wall sector signals (mode transmission experiments) are then presented. The observed mode frequencies are found to be in good agreement with numerical predictions. Next, measurements of the plasma density compression and expansion resulting from these modes are presented. Finally, measurements of the mode damping rate, at amplitudes similar to the ones used for the rotating wall, are presented; the damping rate is found to be fairly constant as a function of temperature, in disagreement with predictions of linear Landau damping for small amplitude waves.

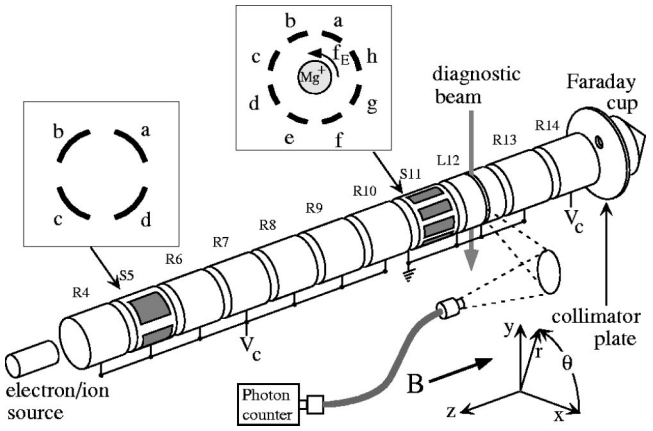

FIG. 1. Schematic of the IV Penning–Malmberg trap used for electron and ion plasma experiments. Electrons are typically confined in the region S5 →S11; Mg^+ ions (shown) are typically confined in the region S11→R13. A laser diagnostic is used for ion plasmas; a collimator plate and Faraday cup diagnostic is used for electron plasmas. Azimuthally-dependent modes are driven and detected with sectored rings (S5 and S11).

II. EXPERIMENTAL SETUP

A schematic of the ''IV'' ion trap is shown in Fig. 1. This Penning–Malmberg trap consists of conducting cylindrical rings carefully aligned along a uniform magnetic field. The rings have inner radius $R_w=2.86$ cm and length $L_{\text{ring}}=5.84$ cm (including the 0.13 cm gap between rings). For the data presented here, the magnetic field strength is $B=4$ T. The entire electrode structure is contained in an ultra-high vacuum chamber with $P\approx 4\times 10^{-9}$ Torr (97% H_2). The rings S5 and S11 are azimuthally segmented to allow for launching and detection of azimuthally-dependent modes; end-on schematics (viewed from the source) of these azimuthal sectors are illustrated in Fig. 1. The ring L12 is slotted to allow for passage of laser light and the detection of ion fluorescence; illustrations of a perpendicular diagnostic laser beam and the fluorescence-detection optics are included in Fig. 1.

Electrons or ions are confined axially by creating a monotonic potential well in the axial direction. In a typical electron experiment, ring R4 and rings L12 through R14 are biased to $V_c=-200$ V, while S5 through S11 are grounded, so that electrons are trapped in the potential well S5→S11, while ions escape out the ends of the trap. In a typical ion experiment, shown in Fig. 1, R4→R10 and R14 are biased to $V_c=+200$ V, while S11→R13 are grounded, so that ions are trapped by the potential well S11→R13. To inject the particles, the left end (R4→R10) of the potential well is grounded, ions or electrons from a source to the left of R4 enter the trap along the magnetic field, and then the left end of the potential well is raised to trap the particles. Typically, about $N_{\text{tot}}\simeq 10^9$ particles are trapped. For ion experiments, a metal vacuum vapor arc (MEVVA) is used to create Mg^+ ions, while for electron experiments, a hot thoriated tungsten filament is used to create free electrons. In both cases, the particle source is located about 100 cm to the left of R4 in the fringing field, $B_{\text{source}}/B\approx 1/90$; this is not shown to scale in Fig. 1.

The plasma length is adjusted by changing the number of rings in the grounded containment section. For these long plasmas, the plasma length is approximately the length of the confining region minus one ring, that is $L_p \simeq (N_{\text{rings}}-1)\times L_{\text{ring}}$, so a plasma trapped in the region S5→S11 is about $6\times L_{\text{ring}} \simeq 35$ cm long. The ring S11, which is used to launch and detect waves, is usually located at one end of the plasma column.

A. Rotating wall fields

Modes are driven in the plasma by applying sinusoidal voltages to one or more of the eight isolated wall sectors on S11. Each of these sectors has axial length $L_s = 3.81$ cm, azimuthal extent $\Delta\theta_s = 27$ degrees centered at $\theta_j = 360(j/8) + 67.5$ degrees; and the sectors are separated azimuthally by frame elements 14 degrees wide. For example, $m_\theta = 0$ modes are driven by applying the same signal to all of the sectors and to the frame. For the standard rotating wall setup, the eight sector voltages are phased so as to create a forwards-rotating $m_\theta = 1$ or $m_\theta = 2$ perturbation at signal frequency f_s, and the frame is grounded. That is, voltages $\Phi_{wj} = A_w \cos(m_\theta \theta_j \pm 2\pi f_s t)$ are applied to the eight wall sectors to create a potential perturbation which rotates in the same direction as the (electron or ion) plasma. Higher-order m_θ harmonics resulting from the azimuthal step-function approximation are small in amplitude and can be ignored in these experiments. We note that the sinusoid at frequency f_s makes a ''wall'' perturbation which rotates at rate $f_w = f_s/m_\theta$.

The driven plasma modes are detected by listening to the azimuthal wall sectors with either a spectrum analyzer or a lock-in amplifier. Typically, the sectors on ring S5 are used to detect the waves launched from ring S11. Normally, a single sector of S5 is used, although for some experiments, such as for distinguishing between odd and even m_θ modes, two opposing sectors are used together. When the confinement length does not include S5, ring S11 can be used for both launching and detecting waves. By applying a sine wave to S11a, for example, and applying the opposite phase signal to S11e, both direction ($m_\theta = +1$ and $m_\theta = -1$) modes are launched in the plasma. The resulting plasma waves can be detected by listening to S11c or S11g; in this case, the intervening sectors (S11b, S11d, S11f, and S11h) are grounded to reduce direct coupling between the drive and detection sectors.

The effect of the rotating wall drive is quantified by either measuring the rate of change of central plasma density (i.e., $\dot{n}_0/n_0$), or by measuring the rate of change of the total angular momentum of the plasma. The total angular momentum P_θ is given by[13]

$$P_\theta = \sum_j \left(m v_{\theta,j} r_j - eBr_j^2/2c\right)$$

$$\simeq -eB/2c \sum_j r_j^2 \equiv -(eB/2c)\langle r^2\rangle, \qquad (1)$$

where the sum is over the N_{tot} particles in the plasma. The plasmas considered here have relatively low density and temperature, so the angular momentum in the electromagnetic field dominates, and the angular momentum is proportional to the mean-square radius $\langle r^2\rangle$. Torques on the plasma thus cause $\langle r^2\rangle$ and generally n_0 to change. For a plasma which evolves self-similarity, one would find $\dot{n}_0/n_0 = -\langle \dot{r}^2\rangle/\langle r^2\rangle$. In practice, we typically observe $\dot{n}_0/n_0 = -\alpha\langle \dot{r}^2\rangle/\langle r^2\rangle$ with $1/2 \lesssim \alpha \lesssim 2$. Thus, measuring the rate of change of central density gives an approximate, but generally adequate, measure of the torque on the plasma.

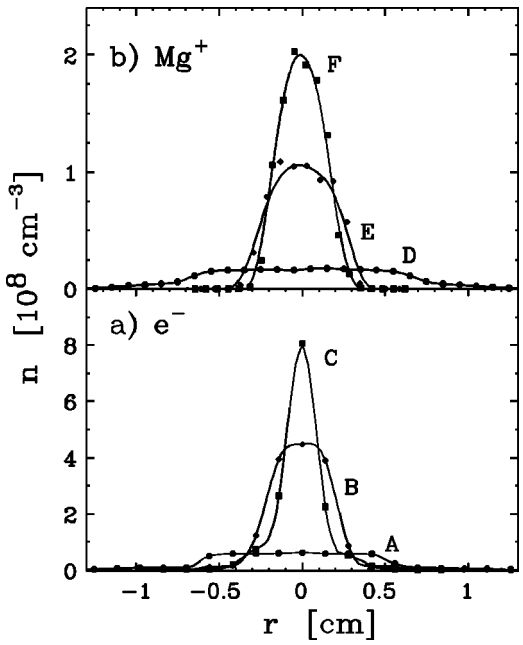

FIG. 2. Measured electron and ion density profiles, demonstrating rotating wall compression and expansion.

B. Electrons

Normally, electron plasmas are trapped in the region S5 →S11, corresponding to a plasma length $L_p \simeq 35$ cm. The plasma radius is typically $R_p \simeq 0.25$ cm, and the central density is typically $n_0 \simeq 4.5\times 10^8$ cm^{-3}, corresponding to $N_{\text{tot}} \simeq 3\times 10^9$ electrons.

The electron plasma measurements consist of a standard inject/hold/manipulate/dump cycle. The plasma is first injected, then held for several seconds so it can relax towards a cooled, near-thermal equilibrium state. The plasma is then manipulated (e.g., by rotating wall fields), and is finally diagnosed by dumping the plasma axially onto the collimator plate and Faraday collector. The radial density profile is obtained from the charge $Q_{\text{FC}}(r,t)$ which passes through a small hole of area $A_h = \pi\ (0.5\ \text{mm})^2$ in the rotatable collimator plate and onto the Faraday cup, as $n(r,t) \equiv Q_{\text{FC}}(r,t)/A_h L_p$. Good shot-to-shot repeatability of the injected plasma is required to obtain a valid profile, and we typically find variability in the central density of $\delta n_0/n_0 \lesssim 0.01$. The charge collected by the collimator plate, Q_{coll}, together with the charge collected by the Faraday cup gives the total charge confined, $Q_{\text{tot}} = Q_{\text{coll}} + Q_{\text{FC}}$.

Figure 2a shows examples of radial electron density profiles $n(r)$ resulting from mode-driven plasma expansion and

compression. For each profile, the symbols indicate measured densities; the lines are smooth fits to the data. Profile B shows a typical electron plasma ($L_p \simeq 35$ cm and $N_{\rm tot} \simeq 2.7 \times 10^9$) measured 5 seconds after injection. Profile A shows the expanded profile which results when a backwards-rotating mode is driven during a 50 second hold; and profile C shows the compressed profile when a forwards-rotating mode is applied. The experimental conditions under which this data was measured will be described in more detail later.

The central plasma temperature T is obtained by slowly dumping the plasma and measuring the collected charge vs confinement voltage.[14] Here, we presume that $T_\parallel = T_\perp \equiv T$, since the electron–electron collision rate $\nu_{\perp\parallel} \equiv \nu_{ee}/2 = \frac{8}{15}\sqrt{\pi} n \bar{v} b^2 \ln(r_c/b) \simeq (1050\ {\rm s}^{-1})(T/1\ {\rm eV})^{-3/2}(n/10^8\ {\rm cm}^{-3})$ is large compared to all other evolution rates. The electrons cool by cyclotron radiation[15] at a rate $\tau_c^{-1} \equiv -\dot{T}/T \simeq 4\ {\rm s}^{-1}(B/4\ {\rm T})^2$, and normally come to an equilibrium temperature of $T \simeq 0.2$ eV, where the cyclotron cooling is balanced by heating from the slow plasma expansion. The rate of background ''mobility'' expansion due to inherent trap asymmetries for these conditions is $\tau_m^{-1} \equiv (-\dot{n}_0/n_0)_{\rm bkg} \approx 3 \times 10^{-3}\ {\rm s}^{-1}$, and the heating rate is approximately $\dot{T}/T \approx (e\phi_0/T)\tau_m^{-1}$, where $e\phi_0$ is the space-charge potential energy per particle at $r=0$.

Energetic plasma electrons can create secondary electrons through collisions with background neutrals, but this rate was found to be negligible for the data presented here. By heating the plasma, we established that at $P \approx 10^{-9}$ Torr the ionization rate $\nu_+ \equiv \dot{N}_{\rm tot}/N_{\rm tot}$ increased exponentially with T, varying from $\nu_+ < 10^{-4}\ {\rm s}^{-1}$ for $T \simeq 0.1$ eV to $\nu_+ \simeq 0.3\ {\rm s}^{-1}$ for $T \simeq 3$ eV. In other experiments with $T \approx 5$ eV, the background ionization replenishes electrons lost to the wall, giving a steady-state electron density.[16]

These electron plasmas often exhibit slow growth of the $m_\theta = -1$, $k_z \simeq 0$ ''diocotron'' mode: over the course of 10 to 100 seconds, the plasma column will drift off-axis and eventually to the wall. To avoid this, two sectors on S5 are used for feedback damping of this mode: the signal from one sector is amplified and phase-shifted, and then applied to the second sector to damp the mode. The $m_\theta = -1$ diocotron mode frequency is $f_d \lesssim 1$ kHz for these electron plasmas, while the $k_z > 0$ Trivelpiece–Gould plasma modes of interest here have frequencies $f_s \approx 1$ MHz, so this negative feedback drive does not adversely affect the rotating wall measurements.

C. Magnesium ions

Referring to Fig. 1, Mg^+ ions are typically confined in the region S11→R13 by biasing rings R4→R10 and ring R14 to $V_c = +200$ V. The normal length of the ion plasma is $L_p \simeq 12$ cm with a radius $R_p \simeq 0.5$ cm and a central density $n_0 \simeq 5 \times 10^7\ {\rm cm}^{-3}$, corresponding to $N_{\rm tot} \simeq 5 \times 10^8$ particles. In the absence of applied perturbations, the plasma expands radially at a background rate $\tau_m^{-1} \approx 5 \times 10^{-4}\ {\rm s}^{-1}$. The ions typically reach an equilibrium temperature of $T \simeq 0.04$ eV, at which point the cooling from collisions with neutrals balances the heating caused by the plasma expansion.

The ion plasmas typically consist of about 70% Mg^+ ions and 30% impurity ions. Based on ion-cyclotron spectroscopy, the impurity ions are believed to be dominantly hydrides of magnesium, i.e., MgH_n^+, where $n=1$, 2, or 3. Isotopically, the plasma consists of approximately 79% $^{24}Mg^+$, 10% $^{25}Mg^+$, and 11% $^{26}Mg^+$.

As with electrons, rotating wall voltages are applied to the plasma using the sectored ring S11, which is usually located at one end of the plasma. These ion plasmas do not exhibit unstable growth of the $m_\theta = 1$ diocotron mode, so no negative feedback is applied.

The main experimental diagnostic for the Mg^+ plasmas[17] is laser-induced fluorescence (LIF), which allows nondestructive local measurement of the plasma density $n(r,t)$, temperature $T(r,t)$, and rotation velocity $v_\theta(r,t)$. This is accomplished by frequency-scanning a continuous 280 nm UV laser beam through one of the $3S_{1/2} \rightarrow 3P_{3/2}$ ''cyclic'' transitions of the Mg^+ ions; and measuring the fluorescence from the ions in a detection volume of 1 $mm^2 \times 3$ mm ($\Delta x \Delta z \Delta y$). In these experiments, the observed fluorescence signal width is dominated by Doppler broadening due to the ion velocities; so $n(r)$, $T(r)$, and $v_\theta(r)$ can be obtained by fitting the scattered photons to three shifted Maxwellians (for ^{24}Mg, ^{25}Mg, and ^{26}Mg). The plasma is essentially unperturbed by this diagnostic, since the laser power is typically less than 1 mW. The diagnostic can be used to obtain both perpendicular and parallel temperatures; however, for the data presented here, the ion–ion ''momentum transfer'' collision rate, $\nu_{ii} = \frac{16}{15}\sqrt{\pi} n \bar{v} b^2 \ln(r_c/b) \simeq (1\ {\rm s}^{-1})(T/1\ {\rm eV})^{-3/2}(n/10^7\ {\rm cm}^{-3})$ is large compared to the neutral cooling rate, $\nu_{iN} \simeq 0.02\ {\rm s}^{-1}(P/4 \times 10^{-9}$ Torr), so the two degrees of freedom are well-equilibrated, i.e., $T_\perp \simeq T_\parallel \equiv T$.

In Fig. 2(b), profile D shows the measured radial density profile, $n(r)$, of an ion plasma ($L_p \simeq 8$ cm and $N_{\rm tot} \simeq 2 \times 10^8$) held in steady-state equilibrium with a $A_w = 1$ V, $f_s = 15$ kHz, $m_\theta = +2$ rotating wall drive. Profile E shows the same plasma after being moderately compressed and profile F shows the same plasma after being compressed by a factor of about 10 in central density n_0. The experimental conditions under which this data was measured will be described in more detail later.

III. TRIVELPIECE–GOULD MODES

Trivepiece–Gould modes were initially derived as a description of normal modes in the electron component of a neutral plasma filling an infinitely long conducting cylinder.[18] Analogous modes also occur in non-neutral plasmas, with the primary difference being a Doppler-shift in the frequencies due to the bulk rotation of the non-neutral plasma column. The unneutralized plasma space charge gives a strong radial electric field, and an **E×B** rotation of the column. At $r=0$, this rotation rate is

$$f_E \equiv \omega_E/2\pi = cen_0/B = 145\ \ {\rm kHz}(n/10^8)(B/1\ \ {\rm T})^{-1}. \tag{2}$$

The diamagnetic and centrifugal contributions to the plasma rotation are small in these experiments, so the total plasma

rotation frequency ω_R is generally close to the **E×B** rotation frequency, i.e., $\omega_R \simeq \omega_E$. In our finite length apparatus, the modes are standing, with density and potential perturbations of the form δn, $\delta\phi \propto \cos(m_\theta\theta - \omega t)\cos(k_z z)R(r)$. Here, $m_\theta = 0, 1, 2, \ldots$, is the azimuthal mode number; $m_z = 0, 1, 2, \ldots$, is the axial mode number, with $k_z \simeq m_z\pi/L_p$; and $m_r = 1, 2, \ldots$, is the radial mode number. The radial eigenfunction, $R(r)$, has m_r interior zeros and falls off to zero at the edge of the plasma (for δn) or at the trap wall (for $\delta\phi$). The modes with azimuthal dependence ($m_\theta \neq 0$) can be launched either in the forward sense (rotating faster than the plasma) or the backward sense (rotating slower than the plasma). Here, we will use the notation $m_\theta = 1, 2, \ldots$, to denote the forwards-rotating modes and $m_\theta = -1, -2, \ldots$, to denote the backwards-rotating modes.

We consider densities small compared with the Brillouin density limit, i.e., $n \ll n_B \equiv B^2/8\pi mc^2$, so these plasmas obey the frequency ordering $\omega_R \ll \omega_p \ll \Omega_c$, where $\Omega_c \equiv eB/mc$.

In this parameter regime, the Trivelpiece–Gould modes can be roughly categorized into three groups: $k_z \simeq 0$ ''diocotron'' modes with (low) frequencies $\omega - m_\theta\omega_R \propto \omega_E$; $k_z \neq 0$ ''plasma'' modes with (intermediate) frequencies $\omega - m_\theta\omega_R \propto \omega_p$; and ''cyclotron'' modes with (high) frequencies $\omega - m_\theta\omega_R \propto \Omega_c$. In this paper, we focus on the intermediate-frequency Trivelpiece–Gould modes.

To predict the frequencies at which these modes occur, we use numerical solutions of the collisionless drift-kinetic equation, which assumes guiding-center **E×B** drifting motion in the azimuthal ($\hat{\theta}$) direction, but keeps the normal kinematics in the axial ($\hat{z}$) direction. Assuming a Maxwellian velocity distribution, Poisson's Equation and the linearized kinetic equations then give the mode equation,[19]

$$\left\{\frac{1}{r}\frac{\partial}{\partial r}r\frac{\partial}{\partial r} - \frac{m_\theta^2}{r^2} - \frac{4\pi m_\theta e c}{rB}\frac{\partial n}{\partial r}\frac{[W(v_\phi/\overline{v})-1]}{\omega - m_\theta\omega_E} - \frac{\omega_p^2}{\overline{v^2}}W\left(\frac{v_\phi}{\overline{v}}\right)\right\}\delta\phi = 0, \tag{3}$$

where $W(z) \equiv 1/\sqrt{2\pi}\int_{-\infty}^{\infty} dx(xe^{-x^2/2})/(x-z)$ is the Ichimaru W-function, and the axial phase velocity is $v_\phi \equiv (\omega - m_\theta\omega_E)/k_z$.

This differential equation in $\delta\phi$ can be solved numerically given an unperturbed density profile, $n(r)$, a wave number k_z, and an azimuthal mode number m_θ. Smooth, physical solutions only exist for discrete eigenvalues of ω, corresponding to different eigenfunctions with radial mode numbers m_r. We use $k_z = m_z\pi/L_p$ for the wave number; this is believed to be a reasonable estimate for the long plasmas studied here, since $R_w/L_p \ll 1$ and numerical simulations of these modes in finite-length geometries find $k_z \simeq (m_z\pi/L)$ with corrections of order (R_w/L_p).[20]

It is often useful to have a simple analytical approximation for the mode frequencies. If we assume a top-hat density profile with $n(r) = n_0$ for $r \leq R_p$ and $n(r) = 0$ for $r > R_p$, take the limits $T \to 0$, $R_w/L_p \to 0$, and assume that $(\omega - m_\theta\omega_E) \to 0$, then Eq. (3) gives the dispersion relation:

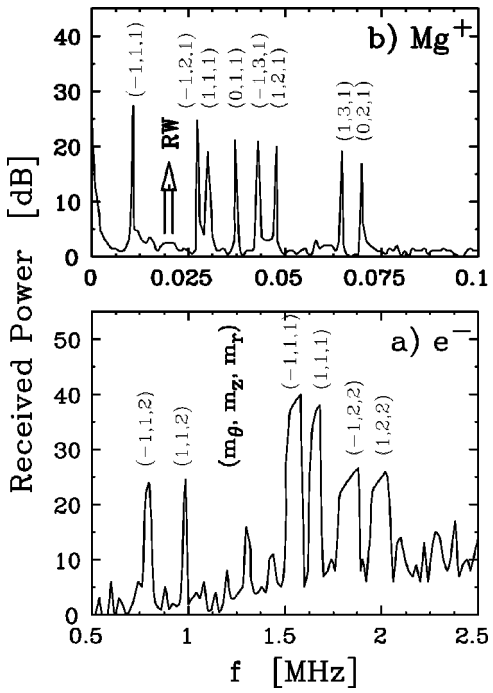

FIG. 3. Mode transmission experiment on electron (a) and ion (b) plasmas. Peaks correspond to enhanced transmission through the plasma of a $m_\theta = \pm 1$ signal launched at frequency f_s. Observed peaks are identified with plasma modes (m_θ, m_z, m_r).

$$\omega - m_\theta\omega_E \simeq A\omega_p R_p k_z\left[1 + \frac{3}{2}\left(\frac{\overline{v}}{v_\phi}\right)^2\right], \tag{4}$$

where

$$A \equiv \begin{cases} \sqrt{\frac{1}{2}\ln(R_w/R_p)}, & m_\theta = 0, \\ \pm 1/j_{m_\theta m_r}, & m_\theta > 0, \end{cases}$$

with a predicted (but not necessarily applicable) linear damping rate,

$$\gamma \simeq -\sqrt{\frac{\pi}{8}}(\omega - m_\theta\omega_E)\left(\frac{v_\phi}{\overline{v}}\right)^3 e^{(-1/2)(v_\phi/\overline{v})^2}, \tag{5}$$

where $j_{m_\theta m_r}$ is the m_rth zero of the m_θth Bessel function.

In these equations, m_θ is assumed to be positive; however, we will use the notation $+m_\theta$ to represent the + sign on the coefficient A (corresponding to modes rotating faster than the plasma) and the notation $-m_\theta$ to represent the − sign on the coefficient A (corresponding to modes rotating slower than the plasma).

A. Mode transmission experiments

Typical mode transmission experiments for electrons and for ions are shown in Figs. 3(a) and 3(b). In Fig. 3(a), $m_\theta = \pm 1$ modes are launched when a signal with frequency f and amplitude $A = 67$ mV is applied to sector S11a, and a 180° phase-shifted signal is applied to S11e. This way, both forwards- and backwards-propagating modes ($m_\theta = \pm 1$) are excited in the plasma. At the other end of the plasma, the received signal on sector S5a is connected to a spectrum

analyzer which automatically tracks the signal frequency, with a bandwidth of 300 Hz. The signal frequency is ramped in 100 seconds from 0.5 to 2.5 MHz.

Figure 3(a) shows enhancements in the received signal of up to 40 dB when the drive frequency corresponds to a plasma mode frequency. The mode identifications in Fig. 3 use the notation (m_θ, m_z, m_r); these identifications are obtained from numerical solutions of Eq. (3). In Fig. 3, the ''noise floor'' is about -130 dB m, corresponding to a received wall voltage of 0.07 $\mu V_{\rm rms}$. Here, ''background'' noise peaks which appear in the absence of a plasma or in the absence of a launched signal have been subtracted from the data. The plasma used here had parameters $L_p \simeq 35$ cm, $R_p \simeq 0.25$ cm, $n_0 \simeq 4\times 10^8$ cm^{-3}, $T \simeq 0.1$ eV, and $N_{\rm tot} \simeq 2.7\times 10^9$; during the 100 second scan n_0 decreased slightly, but $N_{\rm tot}$ remaining constant since $R_p \ll R_w$.

Figure 3(b) shows a similar transmission experiment performed on a magnesium ion plasma. Here, the plasma is kept from expanding by the continuous application of a $f_w = 20$ kHz, $A_w = 0.4$ V, $m_\theta = +1$ phased rotating wall drive using the sectors on S11a, c, e, and g; this balances the inherent asymmetry drag on the plasma by coupling to the (1,1,1) mode, as will be described in the next section. A smaller $m_\theta = \pm 1$, $A = 25$ mV signal is applied using sectors S11b and f, and the signal frequency is ramped from 0 to 100 kHz in 100 seconds while listening to sector S11d with the spectrum analyzer. As for the electron plasma, strong enhancement in the received power is observed when the signal frequency f corresponds to a plasma mode. Here, the received signal at $f = f_w = 20$ kHz is off-scale in amplitude, and has been subtracted from the data along with the background peaks. The plasma used here had parameters $n_0 \simeq 4.3\times 10^7$ cm^{-3}, $L_p \simeq 14.5$ cm, $R_p \simeq 0.66$ cm, and $T \simeq 0.1$ eV.

Verification of the m_θ and m_z mode identifications of Fig. 3 was obtained by varying the antenna geometry used for transmission and reception. For example, the $m_\theta = -1$ modes are no longer observable when a forwards-phased ($m_\theta = +1$) drive is used; similarly, the $m_\theta = +1$ modes are no longer observed when a reverse-phased ($m_\theta = -1$) drive is used. Also, we verified that these $m_\theta = \pm 1$ modes are not excited by a $m_\theta = 0$ or $m_\theta = 2$ drive. For the electron plasma of Fig. 3(a), when driving $m_\theta = \pm 1$ modes and listening with sectors S11f, S11g, and S5d connected together, the odd m_z modes are observed to drop by about 15 dB, while the even m_z modes were observed to rise by about 5 dB. Conversely, listening with sectors S11f, S11g, and S5b connected together causes the even m_z modes to drop by about 15 dB while the odd m_z modes rise by about 5 dB.

Additionally, for the ion plasma, coherent detection of the ion fluorescence at a given mode frequency was used to verify the expected radial mode shapes of the $m_\theta = 0$ and $m_\theta = 1$ modes as well as the odd vs even nature of the $m_z = 1$, 2, and 3 modes.

The $m_\theta = 0$ ion modes seen in Fig. 3(b) are driven by small (unwanted) imbalances in the nominally $m_\theta = \pm 1$ applied signal; $m_\theta = 0$, $m_r = 1$ modes are easily driven in these plasmas. The identification of these modes is obtained from independent transmission experiments using a $m_\theta = 0$ drive, and also from numerical predictions. The associated modes with higher radial mode number, such as (0,2,2) and (0,1,2) are not observed here but are observed when a stronger $m_\theta = 0$ drive is applied to the plasma. For electrons, the (0,1,1) and (0,2,1) modes occur at about 5 and 10 MHz, respectively.

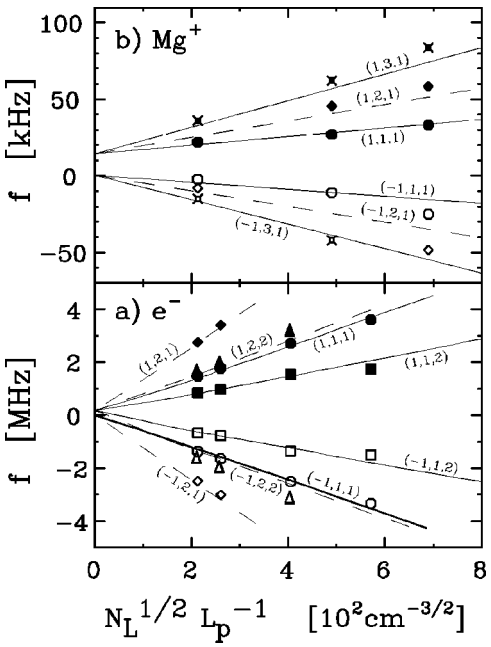

FIG. 4. Observed mode frequencies f of $m_\theta = \pm 1$ modes as a function of plasma length L_p, demonstrating $f - f_E \propto N_L^{1/2} L_p^{-1}$. Measured frequencies (marks) are well-predicted by the numerical solution of modes (lines).

We find that the measured frequencies of $m_\theta = 0$ and $m_\theta = 1$ modes are typically within about 10% of the numerical solutions of Eq. (3); for $m_\theta = 2$ modes, the agreement is typically within 30%. The approximate square profile dispersion relation, Eq. (4), gives the $m_\theta = 0$ mode frequencies to within about 10%, but often differs by 50% or more for the $m_\theta = 1$ or $m_\theta = 2$ modes.

It is of interest to note in Eq. (4) that $\omega - m_\theta \omega_E \propto \omega_p R_p k_z \propto N_L^{1/2} L_p^{-1}$, where $N_L \equiv N_{\rm tot}/L_p$ is the line-charge density. We thus expect the Doppler-shifted mode frequencies to be inversely proportional to plasma length for fixed N_L. This scaling is verified experimentally: in Fig. 4, we plot the mode frequencies observed in transmission experiments versus $N_L^{1/2} L_p^{-1}$. The drive amplitude in these experiments is small ($A_w \leqslant 25$ mV), so the temperature remains low ($T \simeq 0.1$ eV). The symbols correspond to the measured mode frequencies. In Fig. 4(a), electron plasmas with lengths $L_p \simeq 17.5$, 23.4, 35.0, and 40.9 cm were used; the corresponding line-charge density was nearly constant, with $N_L \simeq 10.0$, 9.0, 8.3, and 7.6×10^7 cm^{-1}; and the **E×B** rotation frequency was $f_E \simeq 150$ kHz. The curves through the data are the numerical predictions solutions of Eq. (3); dashed curves represent even m_z modes, while solid curves represent odd m_z modes. It can be seen that the observed modes are reasonably well described by the numerical solutions. Also, the near-linearity of the numerical curves shows that the approximation $\omega - m_\theta \omega_E \propto N_L^{1/2} L_p^{-1}$ is reasonable for these plasmas.

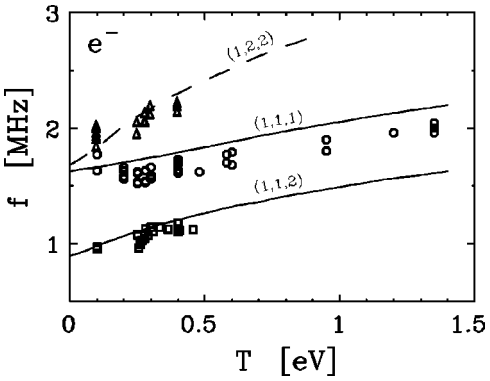

FIG. 5. Scaling of $m_\theta=1$ electron plasma mode frequencies f with plasma temperature T. Measured frequencies (marks) are reasonably well-predicted by a numerical solution (lines).

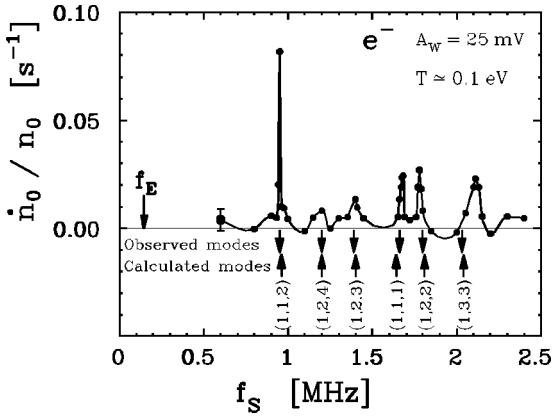

FIG. 6. Measured central density compression rate, $\dot{n}_0/n_0$, for electron plasma as a function of applied $m_\theta=1$ perturbation frequency, f_s, for a small applied signal ($A_w=25$ mV). Observed peaks in plasma compression correspond closely to modes observed in a transmission experiment (down arrows) and to numerically predicted mode frequencies (up arrows), indicating that compression peaks correspond to driven Trivelpiece–Gould modes.

Figure 4(b) shows similar data from Mg^+ plasmas. Here, plasma lengths of $L_p \simeq 8.4$, 12.5, and 17.6 cm were used. The corresponding line-charge density values were $N_L \simeq 3.4$, 2.2, and 1.4×10^7 cm^{-1}, respectively, with $f_E \simeq 14$ kHz. As for electrons, the observed $m_\theta=\pm1$ modes are well-described by both the numerical solutions and by the constant density approximation.

From the $(\overline{v}/v_\phi)^2 \propto T$ term of Eq. (4), it can be seen that a slight upward shift in the mode frequencies is to be expected as the plasma temperature increases. This is found to be true in practice: the observed mode frequencies are seen to shift upward with increasing T. This shift is larger for modes with smaller phase velocities; $m_\theta=0$ modes, for example, which tend to have a larger phase velocity, are observed to shift only slightly with increasing temperature, while $m_\theta=1, m_r=2$ modes, which tend to have a lower phase velocity, are observed to shift more with increasing temperature.

Figure 5 shows the observed frequencies f of three $m_\theta=1$ modes in an electron plasma as a function of plasma temperature T. Aside from the temperature, the parameters are the same as for the plasma used in Fig. 3(a). Plasma heating[21] was obtained by applying a nonresonant sine wave signal on ring R10 at 0.8 MHz at an amplitude $A_w \lesssim 1$ V; this gave plasma temperatures $0.1<T<1.5$ eV. In Fig. 5, it can be seen that the $m_\theta=1$ modes shift upwards slightly as the plasma temperature is increased. The lines in Fig. 5 are the numerical predictions of Eq. (3); it can be seen that the observed temperature variation agrees reasonably well with the numerical solution.

IV. TORQUE FROM DRIVEN PLASMA MODES

We find that all driven $m_\theta=1$ and $m_\theta=2$ modes which are observable in transmission experiments also torque on the plasma and cause plasma heating. As expected, $m_\theta=0$ modes are observed to cause plasma heating but no torque. In this section, we present measurements of plasma expansion and compression resulting from driven $m_\theta=1$ and $m_\theta=2$ modes for electron plasmas and for ion plasmas.

A. Electrons

Figure 6 shows the normalized rate of change of central density, $\dot{n}_0/n_0$, measured on profile B of Fig. 2 as a function of rotating wall drive frequency f_s. Here, a small amplitude ($A_w=25$ mV), forwards-phased $m_\theta=+1$ rotating wall drive is turned on at $t=5$ seconds after inject, and the central density of the plasma is measured as a function of time using the collimator plate and Faraday Cup diagnostic described previously. We then obtain the initial compression rate by fitting to the data for $5<t<6$ sec. This small-amplitude drive creates little heating, so $T\simeq0.1$ eV. The measured background expansion rate of $(\dot{n}_0/n_0)_{\rm bkg}=-0.003$ s^{-1} of this plasma has been subtracted from the data, so the plot indicates compression from the rotating wall alone. The locations of the mode transmission peaks observed on this plasma are shown as down arrows, while the numerically calculated values for the corresponding modes are shown with up arrows. The predicted modes agree quantitatively with the six wave transmission peaks and with the six compression peaks; here, the particle number and temperature were adjusted to $N_{\rm tot}=2.7\times10^9$ and $T=0.1$ eV (compared to direct measurements of $N_{\rm tot}=3\times10^9$ and $T\approx0.2$). Quantitative agreement is obtained between the predicted and observed mode frequencies, and plasma compression is observed from each of the modes.

In practice, significant plasma compression and long-term confinement requires larger-amplitude ($A_w \gtrsim 0.2$ V) rotating wall drives. These larger-amplitude drives cause plasma heating, which in turn results in an upward shift in the plasma mode frequencies. Figure 7(a) shows the same experiment as Fig. 6, but with a larger ($A_w=0.4$ V) rotating wall drive. Figure 7(a) also includes data from the reverse-phased ($m_\theta=-1$) application of the rotating wall drive, which we have here displayed as negative values of f_s. The very low-frequency regime near the diocotron frequency ($f_d \lesssim 1$ kHz) was not investigated due to equipment limitations.

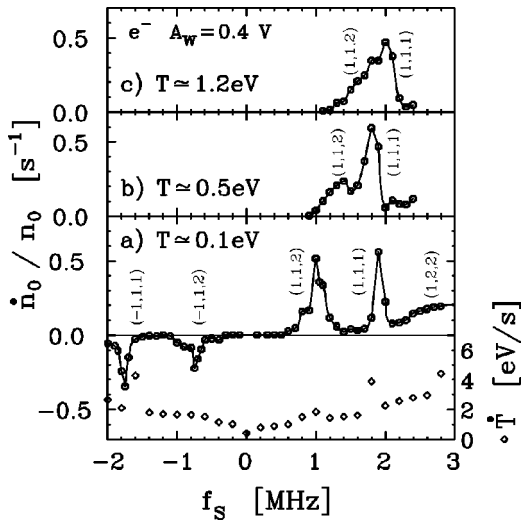

FIG. 7. The measured central density compression rate $\dot{n}_0/n_0$ of electron plasma as a function of applied $m_\theta=1$ drive frequency f_s for plasmas at three different heating levels with a large applied rotating wall signal ($A_w=0.4$ V), demonstrating upward shift and broadening of mode peaks at an increased temperature.

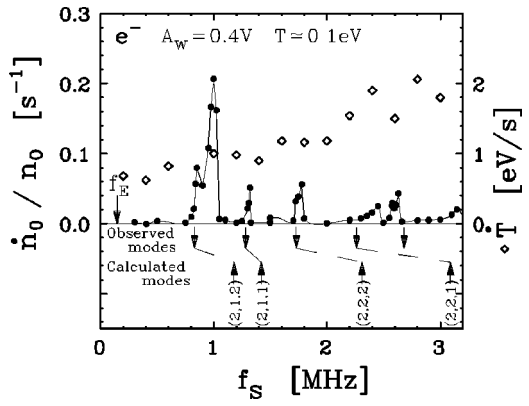

FIG. 8. The measured central density compression rate, $\dot{n}_0/n_0$, for electron plasma as a function of applied $m_\theta=2$ perturbation frequency, f_s. Frequencies of observed compression peaks correspond closely with mode peaks observed in a transmission experiment (down arrows), but are not well-predicted by the numerical solution (up arrows).

It is apparent that backwards-rotating modes cause enhanced expansion, while forwards-rotating modes cause plasma compression; this is consistent with basic thermodynamic arguments.[22] It can also be seen that increasing the amplitude of the rotating wall drive and increasing the plasma temperature has not only increased the magnitude of the torque on the plasma, but has also resulted in frequency shifts and broadening of the mode peaks.

The larger-amplitude drive causes significant plasma heating; the measured initial heating rates for the data of Fig. 7(a) are plotted as diamonds. On the peak of the (1,1,1) mode, for example, the rotating wall drive causes the plasma to heat at a rate of about 4 eV/s up to a maximum temperature of about 2 eV, while on the peak of the (1,1,2) mode, the plasma heats at a rate of about 2 eV/s up to a maximum temperature of about 1 eV.

The upward shift of the mode frequencies in Fig. 7(a) compared to Fig. 6 results primarily from this plasma heating; this is supported by numerical calculations and independent transmission measurements such as shown in Fig. 5. Also, further upward shifts in the mode peaks can be observed if additional external heating is applied to the plasma. In Figs. 7(b) [and 7(c)], the experiment shown in Fig. 7(a) is repeated, but with additional heating from an $A_w=0.12$ V (or 0.3 V), $f_s=0.8$ MHz, $m_\theta=0$ drive on ring R10, which heats the plasma to about 0.5 eV (or 1.2 eV) in the absence of the rotating wall drive.

The correspondence between the observed torque peaks and the mode peaks observed in the transmission experiments was corroborated by repeating the experiment of Fig. 7(a) with the plasma length changed from 35 to 17.5 cm. This change moved the (1,1,2) transmission peak from 0.97 to 1.75 MHz and the measured (1,1,2) torque peak followed, moving from 1.0 to 1.8 MHz. This shift is also reasonably consistent with the numerical solution, which predicts a change from 1.04 to 1.98 MHz.

Driven $m_\theta=2$ modes are also observed to torque on the plasma. The analog of Fig. 7(a), but using a $m_\theta=2$ drive, is shown in Fig. 8. As for $m_\theta=1$, all the modes observed in transmission also cause a measurable torque on the plasma. Here again, down arrows denote modes observed in transmission experiments, while up arrows represent the numerical mode frequency predictions. A comparison with Fig. 7(a) shows that for the same amplitude drive, the torque due to the $m_\theta=2$ modes is about half the magnitude of the torque due to $m_\theta=1$ modes. Presumably, this is a consequence of the $m_\theta=1$ perturbation being larger near the central axis than an $m_\theta=2$ perturbation of the same wall amplitude A_w. The heating rate resulting from driven $m_\theta=2$ modes was also about half as large as observed for a $m_\theta=1$ drive of the same amplitude, perhaps because the effective rotation of the perturbation $f_w \equiv f_s/m_\theta$ is slower for $m_\theta=2$. Enhanced plasma expansion was observed when reverse-propagating $m_\theta=-2$ perturbations were driven, but the negative peaks in $\dot{n}_0/n_0$ were not as distinct as for $m_\theta=-1$, and this regime is not shown in Fig. 8.

B. Ions

Torque peaks measured on ion plasmas are also observed to correspond with Trivelpiece–Gould mode predictions and observations. Figure 9 shows the compression rate obtained from a small-amplitude $m_\theta=+1$ rotating wall drive applied to the Mg^+ ion plasma with $n_0 \simeq 4.6\times10^7$ cm^{-3}, $L_p \simeq 12.2$ cm, $R_p \simeq 0.41$ cm, and $T \simeq 0.06$ eV. The small measured background expansion rate, $(\dot{n}_0/n_0)_{\rm bkg}=-1.4\times10^{-3}$ s^{-1}, is subtracted from the measured compression rate so that the data represents the torque due to the rotating wall only. As with the electron plasmas, there is good agreement between the observed transmission peaks (down arrows) and the plasma compression peaks. The numerically calculated modes (up arrows) show general correspondence with the measurements; but the high axial modes are difficult to predict accurately. Little heating is observed from this small-amplitude drive: the temperature is observed to reach a maximum of about 0.08 eV on a resonance peak.

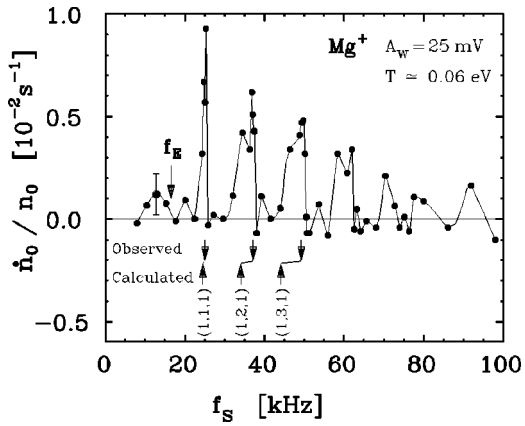

FIG. 9. The measured central density compression rate, $\dot{n}_0/n_0$, for Mg^+ plasma as a function of applied $m_\theta=1$ perturbation frequency, f_s, with a small applied signal ($A_w=25$ mV). Peaks in the compression rate correspond closely to mode peaks observed in a transmission experiment (down arrows); these mode frequencies are reasonably well-predicted numerically (up arrows).

To obtain experimentally useful torques and long-term confinement, larger rotating wall amplitudes ($A_w \gtrsim 0.2$ V) are necessary. Figure 10(a) shows the torque obtained from a strong rotating wall drive ($A_w=0.5$ V) on a somewhat denser plasma ($n_0 \simeq 10^8$ cm^{-3}). Here, we plot the measured total plasma compression $-\langle \dot{r}^2\rangle/\langle r^2\rangle$ as a function of applied rotating wall signal frequency f_s. The arrows indicate calculated mode frequencies for this plasma. It can be seen that the observed broad torque peaks are still consistent with the picture of a rotating wall torque dominated by driven electrostatic modes, but the individual modes cannot be resolved.

Figure 10(b) shows compression data for an externally heated ion plasma ($T \simeq 1.7$ eV) with (total) central density

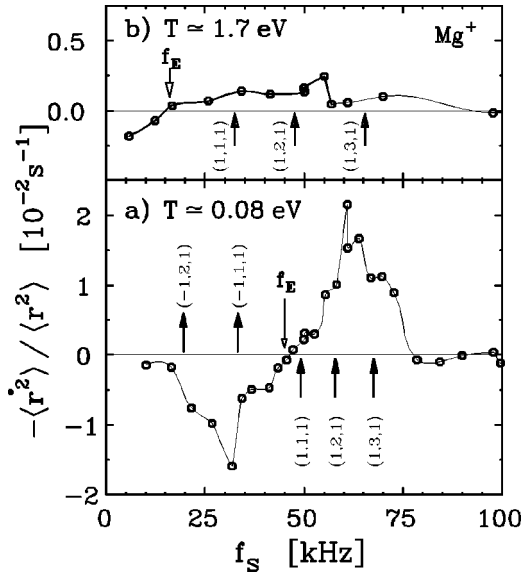

FIG. 10. The measured total compression rate, $-\langle \dot{r}^2\rangle/\langle r^2\rangle$, as a function of the $m_\theta=1$ signal frequency f_s with a large applied signal ($A_w=0.5$ V) for two Mg^+ plasmas differing primarily in their temperature T. Peaks in torque can be seen to correspond to numerically predicted mode frequencies for these plasmas (arrows).

$n_0 \simeq 5.1\times 10^7$ cm^{-3}. The plasma heating has resulted in the torque peaks shifting up in frequency relative to the plasma rotation f_E. Together with the drop in the magnitude of the torque, the upward shift of the mode frequencies as the plasma is heated results in an increased ''slip'' between the applied drive frequency and the resulting equilibrium rotation frequency of a plasma held by the rotating wall drive.

For any given applied frequency f_s, hotter plasmas come to steady-state equilibrium (where the rotating wall torque balances the background drag) at a lower density n_0 and a lower rotation frequency f_E. For the equilibrium plasmas used in Fig. 10, for example, $\Delta f=9$ kHz at $T=0.08$ eV [Fig. 10(a)] vs $\Delta f=32$ kHz at $T=1.7$ eV [Fig. 10(b)], where $\Delta f \equiv f_w - f_E \equiv (f_s/m_\theta) - f_E$.

This is consistent with previous slip measurements (Fig. 3 of Ref. 9), which found that the equilibrium slip frequency between an ion plasma and the rotating wall scaled approximately as the square root of plasma temperature, i.e., $\Delta f \propto T^{1/2}$. The data of Fig. 10 was published previously as Fig. 4 of Ref. 9, without the mode identifications. The broadening due to large amplitude and heating effects hindered the identification of TG modes in the original data.

Previously, the $\Delta f \propto T^{1/2}$ scaling of the equilibrium slip frequency was (mis)interpreted as an indication of field/particle couplings due to bounce-rotation resonances.[9] The present data, such as the narrow compression peaks in Figs. 4–9, clearly show that this Δf scaling is due to the temperature dependence of the (closely-spaced) Trivelpiece–Gould modes; however, with large-amplitude drives, these mode resonances are broadened and overlapping. Thus, the experimental results emphasize the importance of mode resonances, but do not elucidate the microscopic wave/particle coupling mechanisms (such as Landau damping, bounce-rotation resonances, and particle collisions) which cause wave damping and transfer of torque to the bulk particle distribution.

C. Ramped frequency drive

The ability of the rotating wall drive to compress the electron plasma is illustrated in Fig. 11. Here, the squares show measured central density and temperature of a typical electron plasma as a function of the applied frequency f_s for a slow ramp of a $m_\theta=+1$ [Fig. 11(a)], $A_w=0.4$ V rotating wall drive. f_s is ramped linearly from 0.5 to 2.13 MHz in 1000 seconds, starting from the injected profile B of Fig. 2. In the region $0.5<f_s<0.65$ MHz, there is no torque on the plasma [as can be seen in Fig. 7(a)] and the plasma expands slowly; no torque-balance equilibrium is reached yet.

In the region $0.65<f_s<1.95$ MHz, the plasma is being slowly compressed by the (1,1,2) mode; here, the plasma is in an equilibrium state where the mode torque is balancing the background drag on the plasma, i.e., $(\dot{n}_0/n_0)_{rw} + (\dot{n}_0/n_0)_{\rm bkg}=0$. At each of these equilibrium points, the ramp in f_s can be stopped and the plasma held in steady-state confinement.

The range of torque-balanced equilibria obtained in Fig. 11 is quantitatively explained by the compression peaks of Fig. 7 modified by the temperature- and density-induced

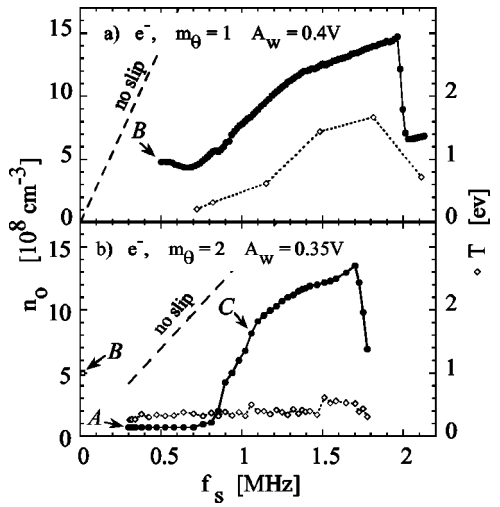

FIG. 11. The measured electron plasma central density n_0 and temperature T resulting from a slow upward ramp of the signal frequency f_s for (a) an $m_\theta=+1$ rotating wall drive or (b) an $m_\theta=+2$ rotating wall drive, demonstrating electron plasma compression by a factor of 20.

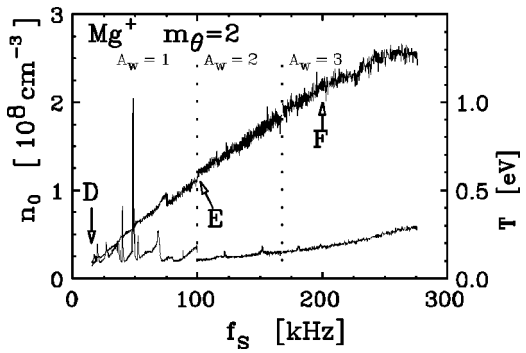

FIG. 12. The measured Mg^+ plasma central density n_0 resulting from a slow upward ramp of the signal frequency f_s for a $m_\theta=+2$ rotating wall drive, demonstrating ion plasma compression by a factor of 15. Peaks in temperature T correspond to $m_\theta=0$ modes driven by slight imperfections in the applied signal.

shifts in mode frequencies. That is, the equilibria of Fig. 11 with $0.65<f_s<1.95$ and $4.5<n_0<14$ represent a torque-balanced equilibrium ''riding up'' the left side of the (1,1,2) peak of Fig. 7. Here, the increasing background drag $[(\dot{n}_0/n_0)_{\rm bkg}\propto n_0^2]$ is balanced by the (increasing) drive torque as f_s approaches the resonant peak at $f(m_\theta,m_z,m_r)$. The ''crash'' at $f_s=2$ occurs because the drive at peak supplies insufficient torque, so the plasma expands until a new equilibrium is obtained on the left side of the next peak; presumably the torque is then from the (1,2,2) mode. The heating resulting from the increasing applied torque causes the mode to shift upwards in frequency, as was demonstrated in Fig. 7, so there is a relatively smooth transition to the region $1.4<f_s<2$ MHz, where the plasma is being compressed by the both the (1,1,2) mode and the (1,1,1) mode.

A similar electron plasma experiment but using a $m_\theta=+2$ drive is shown in Fig. 11(b). Here, however, the drive frequency ramp was begun from an initially expanded plasma, corresponding to profile A of Fig. 2. This expanded plasma was obtained from the injected profile B by applying a $m_\theta=-2$ perturbation at 1 MHz for 50 seconds. A $m_\theta=+2$ drive was then ramped from 0.3 to 1.8 MHz in 415 seconds. Again, consistent with Fig. 8, no compression is observed for the beginning of the frequency ramp ($0.3<f_s<0.8$ MHz), but compression occurs when the rotating wall ramp approaches the frequency of the (2,1,2) mode ($f_s\approx 0.8$ MHz). Profile C of Fig. 2 was taken after ramping to $f_s=1.05$ MHz. As in the $m_\theta=+1$ ramp, a fairly smooth density compression is obtained.

A ramp of ion plasma density is shown in Fig. 12. Here, we plot central density n_0 and temperature T measured during a slow upward frequency ramp of a $m_\theta=+2$ rotating wall perturbation. The ramp begins with a typical ion plasma (profile D of Fig. 2) held with $f_s=15$ kHz, after which the applied frequency f_s is increased from 15 to 280 kHz at a rate of about 20 seconds per kHz. A short $L_p\simeq 8$ cm ion plasma was used here, and A_w was increased from 1 to 2 to 3 Volts during the frequency ramp to maintain plasma compression. The spikes in the temperature at lower f_s are caused by $m_\theta=0$ modes launched by small unwanted imbalances in the rotating wall voltages applied to the 4 azimuthal sectors. Profiles E and F of Fig. 2 are taken at $f_s=100$ and 200 kHz, respectively, of this ramp.

This frequency ramp is sufficiently slow that each point on the curve indicates an equilibrium state where the rotating wall torque is balanced by the background torque; the ramp can be stopped and the plasma held steady-state at any point. This technique has been used to hold ion plasmas in a desired steady-state equilibrium for periods of up to two weeks. Similar results to Fig. 12 are obtained using a $m_\theta=+1$ rotating wall on ion plasmas.

In both electron and ion plasmas, we find an upper limit in the density n_0 to which a given plasma can be compressed. This seems to indicate that the mode-driven torque increases more weakly with increasing density n_0 than the background drag. Measurements on electron plasmas are consistent with this model: we observe a mode-driven compression rate which decreases slightly as n_0 is increased; whereas the background expansion rate is observed to increase strongly with n_0, scaling as $(\dot{n}_0/n_0)_{\rm bkg}\propto n_0^2$. In the ion plasmas discussed here, however, no clear density dependence was observed in mode-driven compression or in the background drag. It is possible that the plasma heating associated with the rotating wall compression is important in limiting the maximum compression of ion plasmas: measurements such as Fig. 10 indicate a decrease in the amplitude of the mode-driven torque with increasing temperature in ion plasmas, while surprisingly no clear temperature dependence of the background drag is found. Normally, we attain a maximum central density in ion plasmas of about $n_0\simeq 0.2\,n_B$; with the application of laser cooling, $n_0\simeq 0.25\,n_B$ was achieved.

A summary of the ion and electron equilibria obtained by slowly ramping the frequency of the rotating wall is shown in Fig. 13. The ions reach a density $n_0\simeq 0.1\,n_{\rm Bi}$; note that with shorter ion plasmas, densities up to $n_0=0.23\,n_{\rm Bi}$ were obtained. The slip in the ion case is much smaller than in the electron case. This is expected, since Eq. (4) suggests

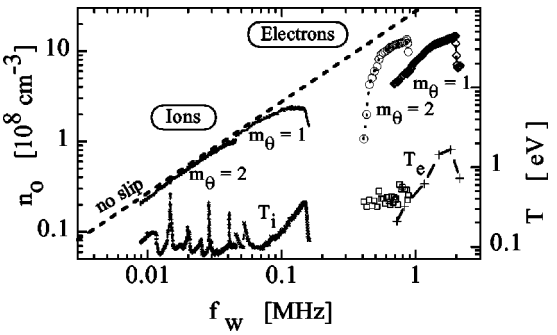

FIG. 13. Central density n_0 versus ramping rotating wall frequency $f_w = f_s/m_\theta$ for electrons and ions using $m_\theta = 1$ and 2; and measured temperature T during ramp.

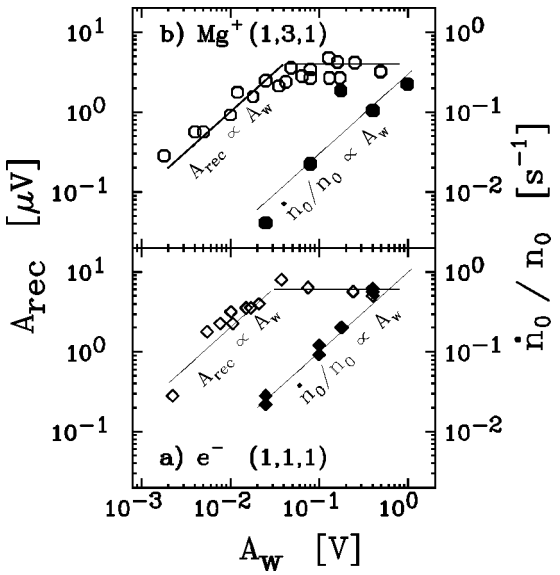

FIG. 14. The peak density compression rate $\dot{n}_0/n_0$ and amplitude $A_{\rm rec}$ of the received signal in mode transmission as a function of drive amplitude A_w for electron plasma (a) and ion plasma (b).

that the slip is proportional to the plasma frequency, and $\omega_{pe} \simeq 210\ \omega_{p\mathrm{Mg}+}$. The ion temperature exhibits peaks that we identify as $m_\theta = 0$ TG modes due to a weak (undesired) $m_\theta = 0$ component of the rotating wall drive. For the electrons, no similar peaks were observed because the first $m_\theta = 0$, $m_r = 1$ TG mode is above 2 MHz.

D. Torque scaling

For drive amplitudes creating a measurable compression, we find a mode-driven compression rate which scales like the first power of the applied drive amplitude. In contrast, simple perturbation theory suggests that the compression should scale as $(\dot{n}_0/n_0) \propto \delta n \cdot \delta\psi \cdot \cos(\phi)$ where δn is the plasma density perturbation (with $\delta n \propto A_{\rm rec}$, where $A_{\rm rec}$ is the rms voltage amplitude received on a wall sector in a transmission experiment), $\delta\psi$ is the applied potential perturbation (with $\delta\psi \propto A_w$), and ϕ is the phase shift between δn and $\delta\psi$ (with measurements showing $\phi \approx$ const). However, since the density perturbation is observed to be saturated ($\delta n \propto$ const) for $A_w > 0.03$ V, the observation that $\dot{n}_0/n_0 \propto A_w^1$ is consistent with this theory perspective.

This is shown more explicitly in Fig. 14, where we plot the measured compression rate $\dot{n}_0/n_0$ as a function of drive amplitude for electrons and for ions. Figure 14(a) shows compression due to the (1,1,1) mode in a typical electron plasma (profile B of Fig. 2). The drive frequency f_s is tuned to the peak of the mode, at $f_s \simeq 1.6$ MHz. The measured compression rate is approximately linear in an applied signal, i.e., $\dot{n}_0/n_0 \propto A_w$. For comparison, the amplitude of the signal received in transmission experiments under the same experimental conditions are shown as open diamonds. It can be seen that the received signal is roughly proportional to the drive amplitude, i.e., $A_{\rm rec} \propto A_w$ for $A_w < 0.02$ V. For $A_w > 0.03$ V, however, the received signal is roughly constant, i.e., $A_{\rm rec} \propto A_w^0$.

A similar result is seen in ion plasmas, as shown in Fig. 14(b). Here, the drive is tuned to the peak of the (1,3,1) mode. It can be seen that the measured compression rate is roughly linear in A_w; the received signal, however, is linear in A_w at low drive amplitudes ($A_w < 0.03$ V), but saturated at higher drive amplitudes.

The mechanism for this mode saturation is not understood at present. Estimates of the mode amplitude corresponding to the maximum received signal, $A_{\rm rec} \simeq 5\ \mu$V for the plasmas of Fig. 14, give $|\delta n/n| \approx 0.01$ to 0.10. The mode amplitude was estimated in some ion plasmas from the LIF signal which oscillates coherently with the mode; these measurements give a maximum perturbation $|\delta n/n| \approx 0.01$. Also, careful observation of the parallel ion velocity distribution function has not revealed any measurable deviation from a parallel Maxwellian for the range of plasma temperatures relevant to this paper.

We believe that the angular momentum of a Trivelpiece–Gould mode is transferred to the particles by a mechanism closely related to mode damping, so predicting the torque resulting from a driven mode requires an understanding of the mode damping rate. Here, we present measurements of the damping rate of large amplitude (1,3,1) modes in a typical ion plasma ($n_0 \simeq 3 \times 10^7$ cm^{-3}, $L_p \simeq 12$ cm). The damping rates were obtained by driving the peak of mode with a $m_\theta = +1$ drive for about 0.2 seconds; the received signal was typically observed to saturate within 10 ms. The drive was then turned off and the rate at which the received signal $A_{\rm rec}$ decreased was observed to be reasonably well-fit by an exponential decay, i.e., $A_{\rm rec}(t) = A_{\rm rec}(0)e^{-\gamma t}$.

In Fig. 15, we plot the measured mode quality $Q \equiv \omega/2\gamma$ as a function of temperature T. We find that $Q \approx 10^3$ for $T > 0.1$ eV, increasing to $Q \lesssim 10^4$ for $T < 0.1$ eV. In this experiment, the plasma temperature was varied in two fashions: either by varying the amplitude of the mode drive A_w, or by fixing A_w and applying varying levels of ion-cyclotron resonance heating. In the first method, the amplitude of the $m_\theta = 1$ drive was varied from $A_w = 1.4$ to 330 mV to provide plasma temperatures ranging from $T = 0.05$ to 0.4 eV. In the second method, the amplitude of the drive was fixed at $A_w = 100$ mV and a signal at the ion cyclotron frequency Ω_c was applied to one sector on S11. The amplitude

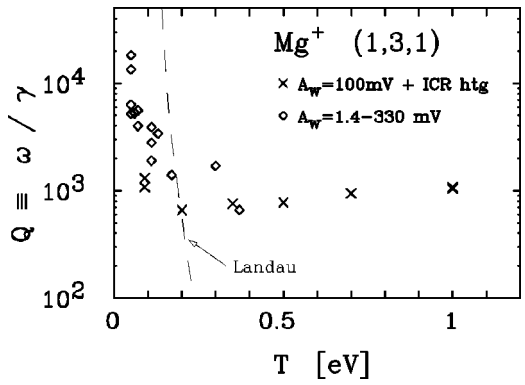

FIG. 15. Measured damping of the (1,3,1) mode in Mg^+ plasma as a function of temperature. Observed damping disagrees markedly with the prediction of linear Landau damping (dashed line).

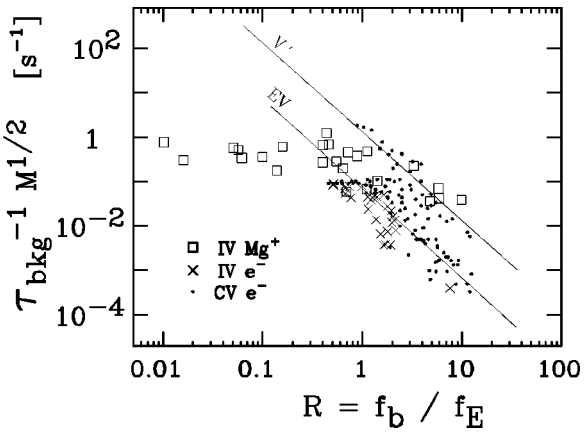

FIG. 16. Measurements of the free expansion rate τ_{bkg}^{-1} resulting from inherent trap asymmetries as a function of plasma rigidity R (axial bounce frequency divided by rotation frequency) for four different apparatuses, demonstrating $\tau_{bkg}^{-1} \propto R^{-2}$ scaling for electron data and anomalous $\tau_{bkg}^{-1} \propto$ const scaling for ion data.

of the cyclotron-frequency signal was varied from 0 to 130 mV to provide various levels of ion-cyclotron resonance heating; corresponding equilibrium temperatures ranging from 0.08 eV to 1.0 eV were obtained.

For comparison to the data, the estimate of linear Landau damping [Eq. (5)] for this mode is plotted. It is apparent that for the amplitude used here the observed mode damping is not described by the simple linear Landau damping model. Recent measurements of the damping rate of $m_\theta = 0$ TG modes obtain similar damping rates.[23,24] Moreover, the damping is seen to be much greater (and in agreement with the linear Landau damping prediction) when $A_w \leqslant 100\ \mu$V; at larger amplitudes, trapping oscillations are observed, and the damping rate is reduced.[23] Preliminary damping experiments done on the (1,1,1) and (1,1,2) modes in a typical electron plasma find a mode quality $Q \simeq 2\times10^3$ to 6×10^3, which is similar in magnitude to the values shown here.

E. Background transport

Measurements of the background transport rate in these traps is relevant to the work presented here in that the principal use of the rotating wall is to counteract background transport. Additionally, mode-enhanced drag may play an important role in the background transport of these plasmas. For the plasmas discussed here (large plasma length L_p and low neutral pressure P), inherent trap asymmetries are believed to be the dominant source of background transport.[4,25] An overview of background transport data of plasmas at low neutral pressure in Penning–Malmberg traps is shown in Fig. 16. Here, we plot the measured background expansion rates τ_{bkg}^{-1} as a function of the plasma ''rigidity'' $R \equiv f_b/f_E = (v/2L_p)/(cen_0/B)$. The rigidity represents the ratio of the individual particle axial bounce frequency to the plasma rotation frequency, and can be expressed as

$$R = 14.6 M^{-1/2} \left(\frac{B}{1\ \mathrm{T}}\right)^{1} \left(\frac{L_p}{10\ \mathrm{cm}}\right)^{-1} \times \left(\frac{n_0}{10^8\ \mathrm{cm}^{-3}}\right)^{-1} \left(\frac{T}{1\ \mathrm{eV}}\right)^{1/2},$$

where $M \equiv m/m_e$ is 1 for electrons and $(210)^2$ for Mg ions. The expansion rates are also scaled by $M^{1/2}$; this mass scaling is valid for most of the particle dynamics, but it is violated by cyclotron radiation effects and by atomic interaction processes.[26]

The two lines represent the range of background expansion rates from early work on two different apparatuses, ''V′'' and ''EV.''[4] The background expansion rate was characterized by τ_m, the time for the central density to decrease by a factor of 2, for plasmas with $n_0 \approx 10^7\ \mathrm{cm}^{-3}$ and $T \approx 1$ eV. The magnetic field B and plasma length L_p was varied, giving the scaling $\tau_m^{-1} = \alpha (B/L)^{-2}$, with $\alpha = 3.1$ for the EV machine and $\alpha = 62$ for the V′ machine. This corresponds to $\tau_m^{-1} = \beta R^{-2}$, with $\beta = 6.7\times10^{-2}$ for EV and $\beta = 1.3$ for V′. As shown by the extent of the lines, these scalings extended over about 5 decades in τ_m, with about a decade of scatter.

The small dots show measured expansion rates τ_m^{-1} for electron plasmas in a cryogenic trap, ''CV.'' For the CV data, the variation in R was accomplished by varying magnetic field B, temperature T, and density n_0, with almost constant plasma length. The data can be seen to be in rough agreement with a $\tau_m^{-1} \propto R^{-2}$ scaling, although a detailed inspection of this data suggests that this scaling is not obeyed for $R < 1$.

The $\times$ symbols in Fig. 16 show $\tau_{bkg}^{-1} \equiv -(\dot{n}_0/n_0)$ for electrons contained in the ''IV'' trap discussed in this paper. For this data, the variation in R was obtained by varying the central density over the range $10^8 < n_0 < 15\times10^8\ \mathrm{cm}^{-3}$, with $B = 4$ T, $L_p \simeq 35$ cm, and $T \simeq 0.2$ eV. We find $\tau_{bkg}^{-1} \simeq (7\times10^{-4}\ \mathrm{s}^{-1})(n_0/10^8\ \mathrm{cm}^{-3})^2$, giving $\tau_{bkg}^{-1} \simeq (4\times10^{-2}\ \mathrm{s}^{-1})R^{-2}$; however, this scaling has not been verified beyond the limited range shown in Fig. 16.

The squares in Fig. 16 show background expansion rates for Mg^+ ions in the IV apparatus; here we plot the scaled expansion rates $\tau_{\langle r^2\rangle}^{-1} M^{1/2}$ as a function of R, where $\tau_{\langle r^2\rangle}^{-1} \equiv \langle \dot{r}^2 \rangle / \langle r^2 \rangle$ and $M^{1/2} = 210$. For this data, the variation in R is achieved by varying the central density over the range

$10^7 < n_0 < 10^8$ cm^{-3} and the temperature over the range $10^{-3} < T < 2$ eV, with $B = 4$ T and $L_p \simeq 12$ cm. Surprisingly, we find no clear temperature or density scaling in the measured ion expansion rates; this contradicts the scaling obtained for electrons. A possible reason for this discrepancy is the collisionality of the ion plasmas: the electron plasmas have electron–electron collision frequencies which are generally low compared with the thermal bounce frequency, i.e., $\nu_{ee}/f_b < 1$; much of the low rigidity ion data, however, is in the opposite regime, i.e., $\nu_{ii}/f_b > 1$.

The mechanism by which the trap asymmetries couple to these plasmas is not well understood at present. As mentioned earlier, however, these plasmas show enhanced radial loss when applied stationary perturbations coincide with zero-frequency ($m_\theta < 0$) plasma modes.[5,7] Thus it is possible that background transport in these plasmas is enhanced by resonances with zero-frequency modes. As yet, however, no connection has been made between the observed confinement scalings such as $\tau_m^{-1} \propto (B/L)^{-2}$ and the multitude of possible mode resonances.

V. DISCUSSION

The application of a rotating electric field to elongated ($L_p \approx 8 \rightarrow 40$ cm) non-neutral plasmas consisting of $N_{\rm tot} \approx 10^9$ electrons or Mg^+ ions can produce sufficient torque to overcome the background drag, thus allowing for density compression and steady-state confinement. A measurable torque is produced when a length-dependent ($k_z \neq 0$) Trivelpiece–Gould mode is launched by the applied field. At the $(m_\theta, m_z, m_r) = (1,1,1)$ mode, for example, when driven with a drive amplitude of $A_w = 0.4$ V, a central density compression of $\dot{n}_0/n_0 \simeq 0.55$ s^{-1} is observed for a typical electron plasma ($n_0 \simeq 4 \times 10^8$ cm^{-3}), and $\dot{n}_0/n_0 \simeq 0.08$ s^{-1} is observed for a typical ion plasma ($n_0 \simeq 4 \times 10^7$ cm^{-3}). This is much larger in magnitude than the measured background expansion rate resulting from inherent trap asymmetries acting on these plasmas: $(\dot{n}_0/n_0)_{\rm bkg} \simeq -3 \times 10^{-3}$ s^{-1} for electrons and $(\dot{n}_0/n_0)_{\rm bkg} \simeq -1.4 \times 10^{-3}$ s^{-1} for ions.

Far from the observed mode frequencies, the applied field does not create an observable torque; the accuracy of this measurement is approximately $\dot{n}_0/n_0 \approx \pm 10^{-3}$ s^{-1}, so we estimate an on-resonance improvement in plasma compression of at least about 500 for the electron plasma and at least about 80 for the ion plasma. The collective mode coupling contrasts sharply with the single particle picture of ''sideband cooling,'' wherein the energy of single particles is transferred from the magnetron motion into damped axial or cyclotron motion.

Driven modes with azimuthal asymmetry $m_\theta = 1$ and $m_\theta = 2$ are observed to torque and heat both ion and electron plasmas; modes with azimuthal symmetry ($m_\theta = 0$) are observed to cause plasma heating but no torque. Driven modes rotating faster than the plasma provide a positive (compression) torque and driven modes rotating slower than the plasma create a negative (expansion) torque, or drag.

We are only able to create a measurable torque on ion or electron plasmas when driving z-dependent, intermediate-frequency ($\omega \sim \omega_p$, $k_z \neq 0$) Trivelpiece–Gould electrostatic modes. We have not been able to measure a positive torque or achieve steady-state confinement in these plasmas with driven length-independent, low-frequency ($\omega \sim \omega_E$, $k_z = 0$) modes. Also, preliminary measurements show large heating (ion-cyclotron resonance heating) but no torque as a result of driving high-frequency ($\omega \sim \Omega_c$) electrostatic modes in a long Mg^+ plasma. This contrasts with experiments on small, laser-cooled spheroidal plasmas, which observe a torque when driving $k_z = 0$, high-frequency ($\omega \sim \Omega_c$) electrostatic modes.[11]

The frequencies of the observed electrostatic modes are typically well-described by numerically solving the linearized drift-kinetic equation for the measured radial density profile and assuming that the plasma is infinitely long (i.e., ignoring end effects). The mode frequency scaling with temperature, length, and line density is found to agree with the numerical solution. The mode identifications have been verified by antenna geometry tests to verify the odd-vs-even nature of m_θ and m_z and by coherent-LIF measurements of the radial mode shapes.

The measured damping of these modes was found to be small ($Q \equiv \omega/\gamma \simeq 1000$), even for plasmas hot enough to have significant linear Landau damping; this indicates that simple linear Landau damping does not describe the damping of these modes at moderate amplitudes. In the region of experimentally useful drive amplitudes ($A_w \gtrsim 0.02$ V), the measured scaling of the mode torque (approximately linear) and mode perturbation amplitude (approximately constant) as a function of drive amplitude A_w also indicates a nonlinear coupling between the mode and the plasma.

ACKNOWLEDGMENTS

We thank Dr. Ross Spencer for use of his drift-kinetic computer program, Dr. Pei Huang, Dr. Brian Cluggish, Dr. Steven Crooks, Dr. Thomas O'Neil, Dr. Daniel Dubin, Dr. Jason Kriesel, Dr. Robert Pollock, Dr. Travis Mitchell, and Mr. James Danielson for useful discussions and the late Mr. Robert Bongard for excellent technical support.

This work is supported by the Office of Naval Research (ONR N00014-96-1-0239) and the National Science Foundation (NSF PHY-9876999).

[1] T. M. O'Neil, in *Non-neutral Plasma Physics*, AIP Conf. Proc. No. 175, edited by G. M. Bunce (American Institute of Physics, Woodbury, New York, 1988), p. 1.
[2] J. N. Tan, J. J. Bollinger, and D. J. Wineland, IEEE Trans. Instrum. Meas. **44**, 144 (1995).
[3] D. S. Hall and G. Gabrielse, Phys. Rev. Lett. **77**, 1962 (1996); ATHENA Collaboration, K. S. Fine *et al.*, in *Nonneutral Plasma Physics III*, AIP Conf. Proc. 498, edited by J. J. Bollinger, R. L. Spencer, and R. C. Davidson (American Institute of Physics, Woodbury, NY, 1999).
[4] C. F. Driscoll, K. S. Fine, and J. H. Malmberg, Phys. Fluids **29**, 2015 (1986).
[5] D. J. Heinzen, J. J. Bollinger, F. L. Moore, W. M. Itano, and D. J. Wineland, Phys. Rev. Lett. **66**, 2080 (1991).
[6] C. S. Weimer, J. J. Bollinger, F. L. Moore, and D. J. Wineland, Phys. Rev. A **49**, 3842 (1994).
[7] D. L. Eggleston, T. M. O'Neil, and J. H. Malmberg, Phys. Rev. Lett. **53**, 982 (1984); T. B. Mitchell, J. J. Bollinger, X.-P. Huang, and W. M. Itano, Opt. Express **2**, 13 (1998).
[8] T. B. Mitchell, Ph.D. thesis, University of California, San Diego, 1993.

[9]X.-P. Huang, F. Anderegg, E. M. Hollmann, C. F. Driscoll, and T. M. O'Neil, Phys. Rev. Lett. **78**, 875 (1997).
[10]X.-P. Huang, J. J. Bollinger, T. B. Mitchell, and W. M. Itano, Phys. Rev. Lett. **80**, 73 (1998).
[11]T. B. Mitchell, J. J. Bollinger, X.-P. Huang, and W. M. Itano, in *Charged Particles and Fundamental Physics*, AIP Conf. Proc. No. 457, edited by D. H. E. Dubin and D. Schneider (American Institute of Physics, Woodbury, NY, 1998).
[12]F. Anderegg, E. M. Hollmann, and C. F. Driscoll, Phys. Rev. Lett. **81**, 4875 (1998).
[13]T. M. O'Neil, Comments Plasma Phys. Control. Fusion **5**, 231 (1980).
[14]B. R. Beck, Ph.D. thesis, University of California, San Diego (1990); B. R. Beck, J. Fajans, and J. H. Malmberg, Phys. Plasmas **3**, 1250 (1996); D. L. Eggleston, C. F. Driscoll, B. R. Beck, A. W. Hyatt, and J. H. Malmberg, Phys. Fluids B **4**, 3432 (1992).
[15]T. M. O'Neil, Phys. Fluids **23**, 725 (1980).
[16]R. E. Pollock and F. Anderreg, in *Non-Neutral Plasma Physics II*, AIP Conf. Proc. 331, edited by J. Fajans and D. H. E. Dubin (American Institute of Physics, Woodbury, NY, 1994), p. 139.
[17]F. Anderegg, X.-P. Huang, E. Sarid, and C. F. Driscoll, Rev. Sci. Instrum. **68**, 2367 (1997).
[18]A. W. Trivelpiece and R. W. Gould, J. Appl. Phys. **30**, 1784 (1959); S. A. Prasad and T. M. O'Neil, Phys. Fluids **26**, 665 (1983).
[19]R. L. Spencer (private communication, 1998).
[20]J. K. Jennings, R. L. Spencer, and K. C. Hansen, Phys. Plasmas **2**, 2630 (1995).
[21]B. R. Beck, J. Fajans, and J. H. Malmberg, Phys. Rev. Lett. **68**, 317 (1992).
[22]T. M. O'Neil and D. H. E. Dubin, Phys. Plasmas **5**, 2163 (1998), Sec. VI A; S. M. Crooks, Ph.D. thesis, University of California, San Diego, 1995.
[23]F. Anderegg, C. F. Driscoll, and D. H. E. Dubin, ''Thermal excitation of TG modes in a pure electron plasma,'' to be submitted to Phys. Rev. Lett.
[24]J. R. Danielson and C. F. Driscoll, in *Non-Neutral Plasma Physics III*, edited by J. Bollinger (American Institute of Physics, Woodbury, NY, 1999), pp. 214–219.
[25]J. M. Kriesel, Ph.D. thesis, University of California, San Diego, 1999.
[26]C. F. Driscoll, in *Low Energy Antimatter*, edited by D. Kline (Word Scientific, Singapore, 1986), p. 184.